Measurement 290 (2026) 123051

Contents lists available at ScienceDirect

Measurement

journal homepage: www.elsevier.com/locate/measurement

The measurement of machinery sound power level (SWL) with optical cameras: theory and experimental validation

Sofia Baldini [a,*], Elke Deckers [c,f], Hervè Denayer [d,f], Luyao Dong [d,f], Paolo Gardonio [a], Domen Gorjup [b], Dionysios Panagiotopoulos [e,f], Roberto Rinaldo [a], Janko Slavič [b]

[a] Università degli Studi di Udine, Dipartimento Politecnico di Ingegneria e Architettura, Via delle Scienze 206, Udine, 33100, Italy
[b] University of Ljubljana - Faculty of Mechanical Engineering, Askerceva 6, Ljubljana, 1000, Slovenia
[c] KU Leuven - Department of Mechanical Engineering, Division LMSD, Wetenschapspark 27, Diepenbeek, 3590, Belgium
[d] KU Leuven - Department of Mechanical Engineering, Division LMSD, Celestijnenlaan 300B, Leuven, 3001, Belgium
[e] KU Leuven Campus De Nayer, Jan Pieter De Nayerlaan 5, Sint-Katelijne-Waver, 2860, Belgium
[f] Flanders Make@KU Leuven, Leuven, Belgium

A R T I C L E I N F O

Keywords:
Sound radiation measurement
Vibration measurement
Third-octave band SWL
Narrow band Sound power level
Photogrammetry
Multi-view
Frequency triangulation

A B S T R A C T

The measurement of structural borne noise from vibrating sources relies on long-lasting laser vibrometry measurements or complex acoustic measurements carried out either in-situ with sound intensity or acoustic camera probes or in specially dedicated acoustic rooms. This research introduces an additional approach for reconstructing structure-borne sound radiation from optical camera multi-view recordings. The total sound power radiation is obtained by integrating numerically the acoustic sound intensity either on a far-field surface enclosing the radiator or a near-field surface given by the surface of the radiator itself. The sound intensity is derived from the flexural vibration reconstructed with frequency-domain triangulation from 16 sequential camera views and the radiation impedances calculated with a BEM model assuming free-field sound radiation. The near-field approach results into a compact matrix formulation, which can be suitably used to derive the radiation modes of the body. The Introduced method is applied to a model prism box and is validated against ISO 3744:2026 acoustic measurements taken in a semi-anechoic room. The method shows good agreement of both the narrow-band and third octave band sound radiation spectra reconstructed from the camera measurements and from the acoustic measurements, with deviations comprised between 0 and 2 dB in the third octave bands comprised between 250 and 1600 centre frequencies. The proposed method provides an additional in situ approach for reconstructing the sound radiation of optically accessible structures from short-duration full-field video acquisitions, which minimises measurement variability, enables detailed modal reconstruction of the structure sound radiation, and serves as acoustic design tool.

1. Introduction

The accurate estimation of the sound power level (SWL) radiated by machinery housings is central for the design and the development of products with low noise emissions in a variety of fields, including transportation vehicles, domestic appliances, industrial plants, etc. [1,2]. Regulations such as the European Directive 2000/14/EC [3] highlight the social importance of mitigating sound emissions, while research in occupational contexts has shown that inaccurate SWL estimations can lead to significant underreporting of worker noise exposure [4]. SWL-based metrics are widely employed in the automotive [5], maritime [6], aeronautical [7] transportation sectors. For these reasons, SWL has emerged as a key descriptor for regulatory, scientific and technical purposes.

Classical approaches to estimate SWL rely on acoustic measurements performed either in situ, with microphones [2,8–12], sound intensity probes [13,14] or acoustic cameras [15–18], or in controlled laboratory environments such as anechoic and reverberant rooms [2,10,11]. Although standardised and widely adopted, these approaches are affected by several limitations. In-situ measurements often suffer from

* Corresponding author.
E-mail addresses: baldini.sofia@spes.uniud.it (S. Baldini), elke.deckers@kuleuven.be (E. Deckers), herve.denayer@kuleuven.be (H. Denayer), luyao.dong@kuleuven.be (L. Dong), paolo.gardonio@uniud.it (P. Gardonio), domen.gorjup@fs.uni-lj.si (D. Gorjup), dionysios.panagiotopoulos@kuleuven.be (D. Panagiotopoulos), roberto.rinaldo@uniud.it (R. Rinaldo), janko.slavic@fs.uni-lj.si (J. Slavič).

https://doi.org/10.1016/j.measurement.2026.123051
Received 9 April 2026; Received in revised form 5 August 2026; Accepted 30 August 2026
Available online 31 August 2026

background noise, the influence of reflections and reverberation of the measurement space, and limited repeatability, whereas laboratory-based measurements require costly facilities and complex setups [2,19]. Moreover, such acoustic measurements provide limited information on the vibro-acoustic mechanisms that lead to sound radiation, which are often critical in the design phase of quieter structures.

To overcome these challenges, there has been increasing interest in vibration-based methods for sound radiation measurements [20–24], in which the measured structural response is used to obtain the radiated sound power and to investigate the sound radiation mechanisms (see also ISO 7849–1 and ISO 7849–2 [25,26]). In this regard, non-contact optical techniques have gained momentum thanks to their ability to capture full-field vibration data without physically perturbing the system. Among these, laser Doppler vibrometry (LDV) has established itself as a benchmark for precision and reliability [27]. However, LDV measurements typically require point-by-point acquisitions, which makes the reconstruction of the sound radiation prone to errors due to uncertainties generated by the variability of the structure response during long lasting measurement sessions. By contrast, high-speed camera measurements allow the simultaneous acquisition of the full vibration field over the visible surface of a structure, thus, significantly reducing the measurement time and enhancing spatial resolution. Indeed, recently, the idea of using camera measurements to reconstruct the full field vibration and the resulting sound radiation of distributed structures has been proposed and investigated experimentally by Gardonio *et al.* [28–31] for simple structures whose sound radiation can be derived analytically from the vibration field with the Kirchhoff-Helmholtz integral [32–35].

Since the late 1980′s, several camera-based approaches for vibration reconstruction have been explored. Three-dimensional point tracking (3DPT) [36–41] and digital image correlation (DIC) [36,39,41–49] have been widely investigated, which rely on stereo or multi-camera setups to triangulate displacements at the structural surface [50–52]. However, these techniques are rather delicate to implement, as they require precise synchronization [53] and calibration [54–57]. To simplify the acquisition procedure, single-camera multi-view triangulation methods have been introduced recently [58–66]. In particular, the frequency domain triangulation (FDT) technique proposed by Gorjup *et al.* [67] has proven effective for reconstructing vibration spectra directly from multi-view video recordings. This method enables the derivation of dynamic flexibility frequency response functions (FRFs) [68] from high-speed video acquisitions, which can then be exploited for acoustic radiation analysis.

The present study proposes an additional methodology for estimating the SWL radiated by thin-walled structures normally encountered in real applications, which integrates high-speed camera measurements with acoustic simulations. The approach is characterised by three distinctive features. Firstly, its core structure, which derives the total sound power radiation with a simple and compact “near-field matrix formulation”. The formulation combines the Kirchhoff–Helmholtz integral equation for the derivation of the total sound power radiation of a vibrating body [32–35] with the reconstruction of the body full-field vibration from frequency-domain triangulation of camera multi-view acquisitions. The formulation boils down to a simple matrix expression based on the so-called acoustic radiation impedance matrix, which under specific circumstances can be reduced to a radiation resistance matrix [32]. This compact formulation provides a direct and computationally efficient framework for estimating from multi-view camera recordings the total radiated sound power of thin-walled structures with complex geometries, for which no closed-form analytical solution of the Kirchhoff–Helmholtz integral equation is available [32–35]. Secondly the derivation of the body sound radiation matrix for generic open/closed spaces with an acoustic Boundary Element Model (BEM), although an acoustic Finite Element Model (FEM) could be employed too [32]. Thirdly, the reconstruction of both narrow and third octave band spectra of the Sound Power Level (SWL) radiated by the machinery both in open and closed spaces.

The measurement approach proposed in this paper offers some key advantages. Firstly, the possibility of performing the measurements directly on the machinery without the need of moving and re-installing it into costly facilities such as anechoic or reverberant rooms. Secondly, it relies on short full-field video acquisitions such that uncertainties arising from variability of measurement conditions are minimised. Thirdly, the physics of the sound radiation can be thoroughly investigated, for example by contrasting the sound radiation of different areas of the body or by deriving the radiation flexural modes of the whole structure [21,32]. Fourthly, the sound radiation into virtual settings (closed/open spaces with specific geometries and sound reflection/absorption properties, etc.) can be reconstructed offline. Hence, it is expected that this measurement tool could be effectively combined with the classical measurement methods for in-situ and laboratory assessment of the sound radiation by machinery as well as for the design and development of equipment characterised by low or tailored sound emissions. Moreover, it can be used to predict the sound radiation into virtual spaces, offering in this way a means to select the best location where to install/use the machinery as well as to design sound absorption/insultation treatments in the vicinity of the machinery. Indeed, knowing how the vibration field influences the sound radiation both in spatial and frequency domains provides an important tool for Noise, Vibration, and Harshness (NVH) analyses of surface and air transportation vehicles (aircraft, helicopters, trains, cars, ships) and the Noise and Vibration (N&V) classification of domestic appliances and industrial machineries.

It is important to underline that, in addition to these interesting features, the proposed methodology presents some significant issues too. The principal is specific to the optical camera vibration measurement approach, which provides displacement measurements whose amplitude is bound to decrease as the frequency raises. Hence, it is expected, that cameras with high spatial and temporal resolution are mandatory to have good quality vibration measurements that cover a large audio frequency range and a wide range of amplitudes. Also, it is expected that the reconstruction from camera measurement of the vibration field, and thus of the sound radiation, will prove quite challenging in presence of bodies with rather complex geometries involving obstructed surfaces, cables, coatings, etc. Moreover, the implementation of 3DPT or DIC approaches requires the application of markers or a speckle pattern on the surface of the radiating body and the presence of a uniform and adequate lighting. Finally, the measurement setting must allow recordings from enough viewpoints such that the flexural vibration of the whole body can be properly reconstructed. In particular, the method cannot reconstruct the sound radiation from optically obstructed surfaces, although, in general, the sound radiation from these surfaces is also expected to be somewhat attenuated.

The study presented in this paper is focussed on a thin-walled prism box test case, which, although used as a laboratory example, was designed in such a way as it replicates the vibro-acoustic response of typical housings of appliances and industrial machinery, where box-like geometries and sharp edges strongly affect the sound radiation and scattering effects. The vibration field of the prism is reconstructed from single-camera high-speed recordings using FDT, yielding the dynamic flexibility FRFs of the structure. These FRFs are then coupled with a BEM model to compute the free-field acoustic pressure distribution over a far-field radiation surface (see ISO 3744 standard [8,9]) and the surface of the vibrating box itself. The methodology presented in this paper allows the derivation of both narrow-band and one-third octave-band SWL estimates, which are validated against conventional techniques using both scanning LDV and microphone array measurements.

The article is structured into 4 main parts. To start, Section 2 describes the model housing structure and the measurement rig considered in this work. Then, Section 3 describes the details of the introduced method, which calculates the total sound power radiation from numerical integration of the acoustic sound intensity either on a far-field surface enclosing the housing or a near-field surface given by the surface of the housing itself. The sound intensity is derived from the housing flexural vibration reconstructed with frequency-triangulation of multi-view camera acquisitions and the radiation impedances calculated with a BEM model assuming free-field sound radiation. Section 4 shows experimental results where the proposed method has been employed to derive the narrow band and third octave band spectra of the sound power level of the thin-walled box. Finally, Section 5 concludes the study by summarizing the key contributions and emphasizing the advantages of the proposed methodology in practical engineering applications.

2. Test case and measurement setups

To assess the validity of the proposed methodology, three types of measurements were carried out on a model machine housing. The first measurement approach relied on a high-speed camera setup to implement the suggested optical approach to reconstruct the flexural vibration fields of the box surfaces and then the total sound power radiation. The second employed a scanning laser Doppler vibrometer, used to independently validate the vibration field obtained from the camera acquisitions. The third one was performed in a semi-anechoic chamber, where a microphone array was installed according to the ISO 3744 standard [8,9] to measure the total sound power radiation, which served as a benchmark to assess the validity of the proposed sound radiation measurement approach. The box model structure used in this study is presented in Subsection 2.1. Then, Subsections 2.2 and 2.3 describe respectively the camera and laser vibrometer vibration measurement setups and the microphone acoustic classical measurement setup.

2.1. Test machine housing box

Fig. 1 illustrates the thin-walled box structure considered in this study, which consists of three main components: a heavy base disc, a rotating disc and the box structure with flexible lateral and top walls. The heavy base disc is grooved to host the smaller rotating disc, which is fixed to the base via a turning joint. The rotating disc has a rectangular edge on top where the box is fixed. The base disc and the flexible prism form a closed thin-walled shell structure that resembles a machine housing on a rigid floor.

Fig. 1a shows the geometry of the box lateral and top parts with numerical labels assigned to the five flexible faces. The dimensions of the rig are given in Table 1. The box was excited in bending with a shaker located inside the box itself and connected to the face N. 4 (see Fig. 1a) of the prism via stinger equipped with an impedance head that recorded the point force excitation.

2.2. Camera and laser doppler velocimetry measurement setup

The camera recordings were taken with the Photron FASTCAM SA-Z high-speed optical camera shown in Fig. 2b. The scene was illuminated by a Nanlite Forza 720B studio reflector, as well as a custom battery-powered LED reflector to achieve constant and consistent illumination across the whole imaged surface of the box. The camera captures 50,000 12-bit monochrome images at a frame rate of 10,000 frames per second. In this work, 16 videos were recorded with a spatial resolution of 896 × 896 pixels, resulting in a total image dataset of approximately 1 terabyte. To facilitate the Digital Image Correlation (DIC) image processing, a high-contrast speckle pattern was applied to each face of the box as shown in Fig. 2. Two rows of ArUco markers (4x4_72 dictionary, approximately 7 mm in size) were printed at the top and bottom of each pattern to enable the automatic extrinsic calibration of the multi-view imaging system. The box was rotated by fixed seps around its vertical axis between consecutive video acquisitions. This approach allowed high-speed camera recordings of the structure under stationary broadband random excitation from 16 different viewpoints, ensuring that the same excitation signal was used for each measurement. To ensure adequate temporal windows for subsequent spectral averaging, each of these sequential video acquisitions lasted for 10 s. The measurements were conducted in the 200–2000 Hz frequency range, corresponding to a structural wavelength ranging between 0.1 m and 0.3 m. The FRFs acquired from the impedance head mounted on the shaker were monitored throughout the acquisition process to ensure repeatability. In practical applications where there is no control on the vibration field, the sequence of camera acquisitions should be taken in close sequence under stationary working conditions of the machinery. Here, it is important to

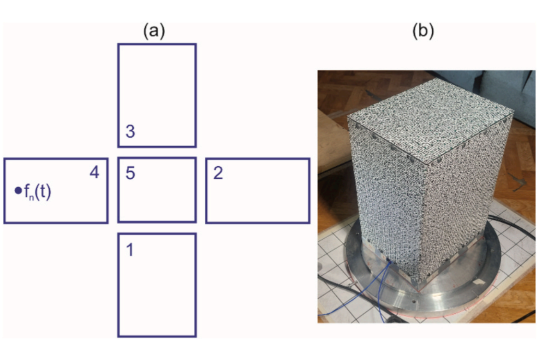

Fig. 1. Thin-walled box structure a) open view with face IDs and shaker position, b) picture of the test structure.

Table 1
Box geometry and mechanical properties.

Component	Geometry and mechanical properties	
Thickness	2 mm	
Material lateral surfaces	Steel	
	Density	$\rho_s = 7500 kg/m^3$
	Young modulus	$E_s = 21E^{10} N/m^2$
	Poisson ratio	$\nu_s = 0.29$
Material top surface	PLA	
	Density	$\rho_{PLA} = 1220 kg/m^3$
	Young modulus	$E_{PLA} = 0.275E^{10} N/m^2$
	Poisson ratio	$\nu_{PLA} = 0.331$
Box face	**Dimension (mm)**	**N° target points**
Face 1	198x320	15x19
Face 2	240x320	12x19
Face 3	198x320	15x19
Face 4	240x320	12x19
Face 5	240x198	15x12

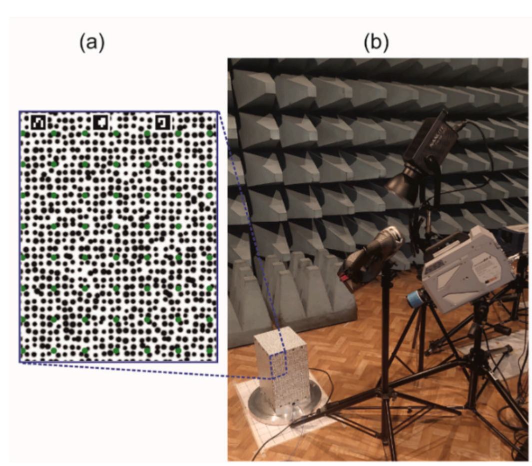

Fig. 2. a) Speckle pattern to digital image correlation procedures with ArUco markers for extrinsic calibration and b) camera measurement setup composed by the thin-walled box structure, a high-speed camera and two light sources.

emphasize that the proposed methodology requires a stationary vibration condition throughout the entire multi-view acquisition process in order to function properly.

The calibration of the multi-view imaging system was conducted in two stages. First, intrinsic camera calibration was performed using images of a standard checkerboard pattern. This step provided reference optical parameters, such as focal length and optical centre, which were incorporated into the intrinsic camera calibration matrix $\mathbf{K}$ [56]. Since the optical system of the camera remained unchanged throughout the entire image acquisition process, this calibration was performed only once. Second, extrinsic calibration was carried out for each of the 16 viewpoints using the Perspective-n-Point algorithm [69]. This was achieved by combining the detected ArUco markers in the recorded images with their known spatial positions on the box surface. As a result, the perspective camera rotation matrices $\mathbf{R}_i$ and translation vectors $\mathbf{t}_i$ were determined for each viewpoint i, yielding a fully calibrated multi-view imaging system with well-defined perspective camera projection matrices $\mathbf{P}_i$ [54]:

$$\mathbf{P}_i = \mathbf{K}[\mathbf{R}_i|\mathbf{t}_i] \tag{1}$$

The vibrations measured from the camera setup were validated against reference measurements obtained using a laser vibrometer as shown in Fig. 3. To facilitate this validation process, as illustrated in Fig. 2a, the speckle pattern decal applied to the box was enhanced with a grid of green circular markers. These markers served as target points for the laser vibrometer measurements and were located at the nodal points of the mesh of triangular elements used for the BEM (see section 3). The flexural vibrations at all marker positions were measured using the laser vibrometer, which was oriented to capture the normal components of the flexural vibrations on each face of the box. The laser system performed an automated scan of the vibration response for the grid of markers on one of the five surfaces before the box was rotated to facilitate measurements on adjacent faces. Only for the measurement of the top surface the laser was repositioned to ensure its measurement axis was set perpendicular to the measurement surface. The laser vibrometer acquired the spectra of the mobility Frequency Response Functions (FRFs) [68] for the normal velocities per unit force excitation, with the excitation provided by the shaker located inside the box.

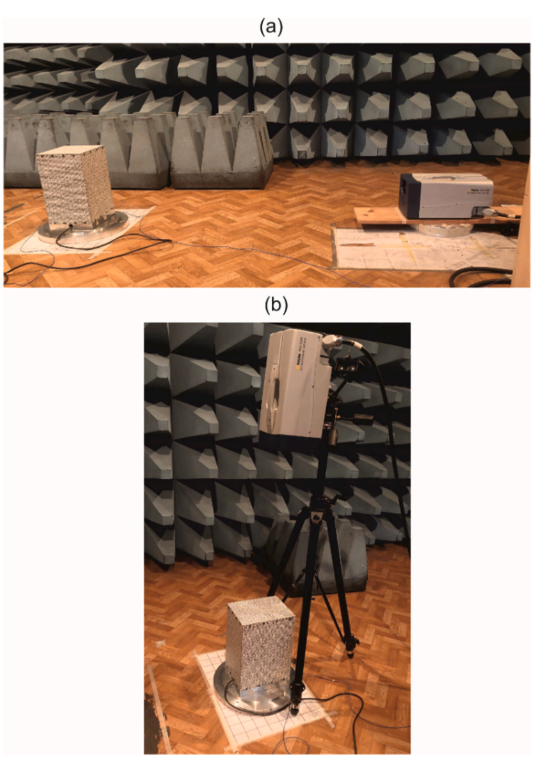

Fig. 3. Laser vibrometer measurement setup a) for lateral surfaces and b) for top surface.

2.3. Classical acoustic measurement setup

The total sound power radiated by the five flexible faces of the box was measured in a semi-anechoic room according to ISO 3744:2026 [8,9]. More specifically, as shown in Fig. 4, FRFs of the radiated sound pressure per unit force excitation were acquired on a grid of 96 positions uniformly distributed on a cylindrical measurement surface. The sound pressures at the 96 positions were measured with the microphone array depicted in Fig. 4b. As done for the camera and the laser vibrometer measurements, the microphone array was kept fixed and multiple measurements were taken after the box was rotated by 45° at each acquisition such that the whole set of 96 measurements points was covered. As anticipated above, the measurements were conducted within the 200–2000 Hz frequency range, corresponding to an acoustic wavelength spanning from 1.72 m to 0.17 m.

3. Sound power level from camera measurements

This section presents the core formulation proposed in this paper, which builds on two milestones. Firstly, the derivation of the flexural vibration field of the body from frequency triangulation of multi-view camera recordings. Secondly, the derivation of the total sound power radiation of the vibrating body from the integral of the sound intensity over a measurement surface that encloses the body itself. Recalling that the sound intensity is a vector quantity given by the product of the acoustic pressure (scalar) and the acoustic particle velocity (vector), in this study two approaches are considered. The first relies on a far-field formulation that, consistent with ISO 3744:2026 requirements [8,9], derives the total sound power radiation by integrating the sound intensity over a far-field surface that encloses the structure, as shown in Fig. 5b. Instead, the second approach builds on a near-field formulation, where the sound radiation is obtained by integrating the sound intensity over the surface of the radiator itself, as shown in Fig. 5a. As discussed in [31], the former formulation takes advantage of the fact that, over the far-field surface, the sound waves locally resemble plane waves with particle velocity oriented in normal direction to the surface and amplitude proportional to the sound pressure. Thus, the total sound power radiation can be calculated directly from the sound pressure over the surface, which, in turn, can be derived from the vibration field of the prism. Instead, the latter formulation exploits the fact that the particle velocity over the radiation surface is bound to coincide with the flexural vibration of the prism. Hence the total sound power radiation can be calculated directly from the product of the vibration velocity and sound pressure fields over the surface of the structure, where the sound field can be derived from the vibration field too [31]. Overall, both approaches rely on the derivation of the radiated sound pressure field respectively over the far-field surface and the near-field surface, that is the surface of the body itself. For bodies with complex shapes this can only be accomplished numerically, with a boundary element or a finite element model. In this study the former has been used although the latter could have been employed too provided the sound radiation into free field was appropriately modelled with infinite elements or other non-reflecting conditions at the boundary of the 3D FEM mesh.

In the remainder of this section, Subsection 3.1 first briefly revises the frequency-domain triangulation technique applied to multi-view image acquisitions to detect the normal displacements of the enclosure. Next, Subsection 3.2 introduces the BEM model [32,70] for the computation of the sound pressure over the far-field and near-field surfaces. Finally, Subsection 3.3 outlines the formulation for the derivation of the sound power level in both narrow-band and 1/3-octave spectra, following the guidelines of ISO 3744:2026 [8,9].

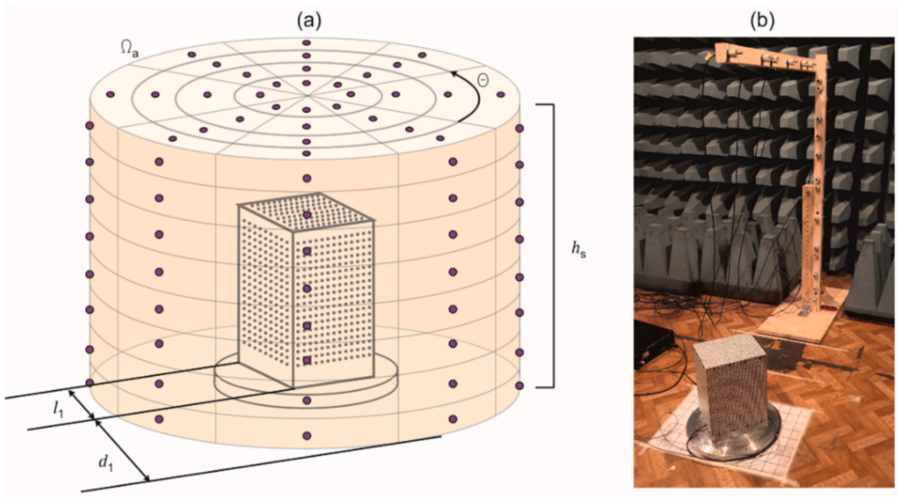

Fig. 4. Setup for acoustic measurements. a) Sketch of the ISO 3744 standard measurement points [8] b) Array of 12 microphones in a semi-anechoic room.

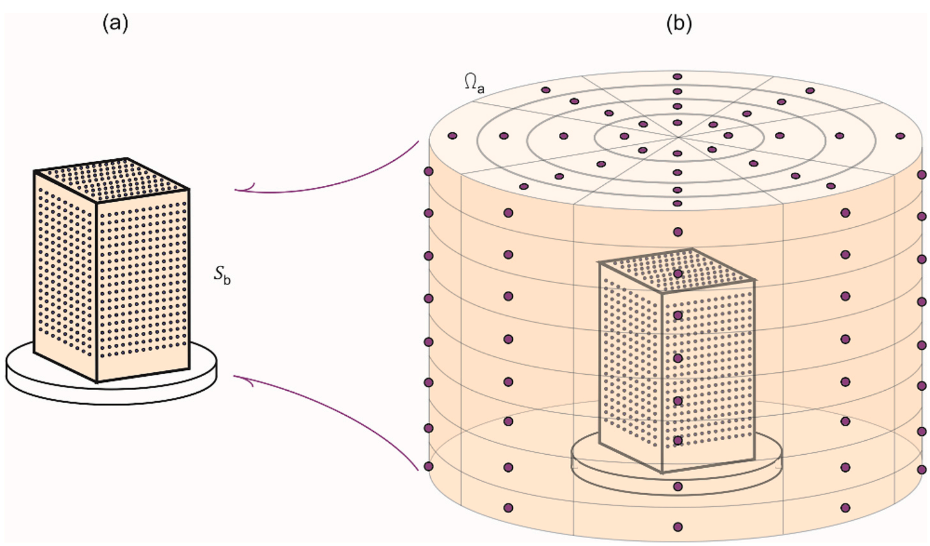

Fig. 5. a) Proposed near-field sound radiation measurement surface built by collapsed the classic far-field sound radiation measurement surface (b) on the box.

3.1. Reconstruction of flexural vibration from camera measurements

The flexural vibration fields of the box radiating surfaces are reconstructed from high-speed video recordings and the frequency-domain triangulation proposed in Ref. [67]. Here, the classical pinhole formulation that links the position of a r-th point $\mathbf{x}_{s,r}$ on the surface of the box structure given in the global reference system with its projection into the image plane of the i-th camera is expressed into the frequency domain with the relation:

$$\mathbf{y}_{\mathrm{i}}(\omega) = \frac{1}{w_{\mathrm{i}}}\mathbf{P}_{\mathrm{i}}\mathbf{x}_{s,r}(\omega) \tag{2}$$

where ω is the angular frequency, $\mathbf{x}_{s,r}(\omega)$, $\mathbf{y}_{\mathrm{i}}(\omega)$ are the Fourier transforms of the homogeneous vectors $\mathbf{x}_{s,r} = \left[x_{s,r}, y_{s,r}, z_{s,r}, 1\right]^T$, $\mathbf{y}_{\mathrm{i}} = [u_i, v_i, 1]^T$ giving the 3D position of the r-th point and its projection into the image plane of the i-th camera and w_{i} is the perspective scale factor. Considering the whole set of image views, the following homogeneous system of equations can be assembled from which the position of the point can be univocally retrieved [65]:

$$\mathbf{D}\mathbf{x}_{s,r}(\omega) = 0 \tag{3}$$

Here, the matrix $\mathbf{D}$ is derived by setting $\mathbf{y}_{\mathrm{i}}(\omega)\times(1/w_{\mathrm{i}})\mathbf{P}_{\mathrm{i}}\mathbf{x}_{s,r}(\omega) = 0$ [31]. In this work, the displacements at the nodal points of the BEM mesh were reconstructed using Lucas–Kanade DIC photogrammetry [71], which exploits the speckled pattern applied to the box. Once the displacement fields were reconstructed, the dynamic flexibility FRF at each nodal point was derived straightforwardly with the following expression [68]:

$$\alpha_r(\omega) = \frac{w_r(\omega)}{f(\omega)} \tag{4}$$

In this equation, $w_{s,r}(\omega) = \mathbf{d}_{s,r}(\omega) \bullet \mathbf{n}_{s,r}$ is the complex amplitude of the displacement in normal direction to the surface of the box at position $\mathbf{x}_{s,r}$, which is retrieved from the 3D displacement given by

$\mathbf{d}_{s,r}(\omega) = \mathbf{x}_{s,r}(\omega) - \mathbf{x}_{s,r0}$, where $\mathbf{x}_{s,r0}$ is the rest position of point $\mathbf{x}_{s,r}$ and $\mathbf{n}_{s,r}$ is the normal to the surface of the box at position $\mathbf{x}_{s,r}$. Also, $f(\omega)$ is obtained from the Fourier transform of the force time-history. The laser vibrometer detects velocities rather than displacements such that mobility FRFs were measured $Y_r(\omega) = \dot{w}_r(\omega)/f(\omega)$ that were then reconducted to dynamic flexibility FRFs recalling that the following relation holds [68]:

$$\alpha_r(\omega) = \frac{Y_r(\omega)}{j\omega} \tag{5}$$

Here $j = \sqrt{-1}$ and $\dot{w}_r(\omega)$ is the complex amplitude of the velocity in normal direction to the surface of the box.

The validity of the proposed camera-based vibration measurement approach has been assessed with respect to the spectrum of the spatially averaged flexural vibration of the whole box, which was expressed in terms of the total flexural kinetic energy:

$$\overline{K}(\omega) = \frac{1}{4}\sum_{f=1}^{5}\int_{\Omega_f} \rho_f h_f \left|\dot{w}(\mathbf{x}_f,\omega)\right|^2 \mathrm{d}\Omega_f \tag{6}$$

Here ρ_f, h_f and Ω_f are the density, thickness and area of the f-th faceplate of the box and $\dot{w}(\mathbf{x}_f,\omega)$ is the complex amplitude of the transverse velocity at position $\mathbf{x}_f$ on the f-th faceplate. Considering the dynamic flexibility FRFs $\alpha_r(\omega)$ reconstructed from the camera measurements, the total flexural kinetic energy was thus derived with the following matrix expression:

$$\overline{K}(\omega) = \sum_{f=1}^{5}\frac{\omega^2 M_f}{4N_f}\boldsymbol{\alpha}_f^{\mathrm{H}}(\omega)\boldsymbol{\alpha}_f(\omega)|f(\omega)|^2 \tag{7}$$

where $(\ )^{\mathrm{H}}$ is the Hermitian-transpose matrix operator, N_f and M_f are the number of measurement points and the mass of the f-th faceplate and the vector $\boldsymbol{\alpha}_f(\omega) = \lfloor \alpha_{f,1}(\omega) \quad \cdots \quad \alpha_{f,F}(\omega) \rfloor^{\mathrm{T}}$ contains the dynamic flexibilities reconstructed at the BEM grid of points of the f-th faceplate of the box from the camera acquisitions. The total flexural kinetic energy was also derived from the laser vibration measurements. Here Eq. (7) was still used, except that the vector with the dynamic flexibility FRFs was built from the vector of mobility FRFs $\mathbf{Y}_f(\omega) = \lfloor Y_{f,1}(\omega) \quad \cdots \quad Y_{f,F}(\omega) \rfloor^{\mathrm{T}}$ measured with the laser vibrometer at the BEM grid of points of the f-th faceplate of the box, such that $\boldsymbol{\alpha}_f(\omega) = \mathbf{Y}_f(\omega)/(j\omega)$.

Before moving into the formulation for the sound power radiation, it is worth noting that the kinetic energy represents a compact, yet informative, descriptor of the structural vibrations, since it directly reflects the contribution of all vibrating surfaces and highlights resonance phenomena through its frequency dependence. Therefore, by analysing its spectral distribution, it is possible to gain an overview of the global flexural vibration response of the box and to assess the capability of the camera-based methodology to reproduce the same vibrational features captured by the reference laser vibrometer measurements. To have a full account of the flexural response of the box model structure, the flexural deflection shapes of the flexible walls at the principal resonance frequencies have also been analysed.

3.2. Derivation of total sound power radiation from BEM model

The BEM model developed for the calculation of the radiated sound field was built using the open-source software of Ref. [72]. The model relies on a mesh of triangular BEM elements that covers the surfaces of the box and of the basement discs visible in Fig. 1 for example. The model is built in such a way as to impose a rigid floor boundary condition and free-field sound radiation into half space, which resemble the acoustics of the semi-anechoic room used to validate the proposed methodology (see Fig. 3a,b and 4b). To achieve the necessary computational accuracy, the element density criterion discussed in [73,74] was strictly enforced, ensuring that the mesh contained at least six elements per half-wavelength at the highest frequency of interest. This criterion is essential to accurately capture the spatial variations of the acoustic field and to prevent numerical dispersion errors. In addition, triangular elements were chosen to improve the convergence of the solution [70]. The software implements the classical BEM collocation approach (see Ref. [32,73] for more details) assuming the complex sound pressure $p(\xi,\eta,\omega)$ and complex transverse velocity $\dot{w}(\xi,\eta,\omega)$ within each triangular element are given by the following relations in the normalised coordinates ξ,η:

$$p(\xi,\eta,\omega) \approx \sum_{n=1}^{3} N_n(\xi,\eta)p_n(\omega) = \mathbf{N}(\xi,\eta)\mathbf{p}_{\mathrm{se}}(\omega), \tag{8}$$

$$\dot{w}(\xi,\eta,\omega) \approx \sum_{n=1}^{3} N_n(\xi,\eta)\dot{w}_{\mathrm{n}}(\omega) = \mathbf{N}(\xi,\eta)\dot{\mathbf{w}}_{\mathrm{se}}(\omega), \tag{9}$$

where the vectors $\mathbf{p}_{\mathrm{se}}(\omega)$ and $\dot{\mathbf{w}}_{\mathrm{se}}(\omega)$ encompass the sound pressures and transverse velocities at the three nodes of the e-th BEM element and the vector $\mathbf{N}(\xi,\eta) = \lfloor N_1(\xi,\eta) N_2(\xi,\eta) N_3(\xi,\eta)\rfloor$ contains the linear shape functions of each BEM element:

$$\begin{cases} N_1(\xi,\eta) = 1-\xi-\eta \\ N_2(\xi,\eta) = \xi \\ N_3(\xi,\eta) = \eta \end{cases} \tag{10}$$

Each shape function $N_n(\xi,\eta)$ is defined such that it has a unit value at the location of node n and it is zero at all other node locations. The acoustic equations for the radiated sound pressure are derived by substituting Eqs. (8) and (9) into Kirchhoff-Helmholtz integral Equation [32]:

$$C(\mathbf{x}_{\mathrm{a}})p(\mathbf{x}_{\mathrm{a}},\omega) = \int_S \left(p(\mathbf{x}_s)\frac{\partial G(\mathbf{x}_s,\mathbf{x}_{\mathrm{a}},\omega)}{\partial \boldsymbol{n}} + j\rho_0\omega G(\mathbf{x}_s,\ \mathbf{x}_{\mathrm{a}},\omega)\dot{w}(\mathbf{x}_s,\omega)\right)\mathrm{d}S \tag{11}$$

using the half-space Green function $G(\mathbf{x}_s,\mathbf{x}_{\mathrm{a}}) = \frac{e^{-jk|\mathbf{x}_s-\mathbf{x}_a|}}{4\pi|\mathbf{x}_s-\mathbf{x}_a|} + \frac{e^{-jk|\mathbf{x}'_s-\mathbf{x}_a|}}{4\pi|\mathbf{x}'_s-\mathbf{x}_a|}$ to have the scattering effect of the rigid floor. Indeed, here $\mathbf{x}'_s$ represents the mirror radiating source location with respect to the floor. Also, $\dot{w}(\mathbf{x}_s,\omega)$ is the complex amplitude of the normal velocity at position $\mathbf{x}_s$ located on the surface of the radiating object S, whereas $\mathbf{x}_a$ represents a position in the unbounded acoustic domain. Finally, ρ_0 is the density of air and $C(\mathbf{x}_a)$ can be equal to -1 or $-1/2$ respectively if the point $\mathbf{x}_a$ is in the unbounded domain or on the radiated surface. Using the collocation approach, the Kirchhoff-Helmholtz integral Equation is turned into a set of algebraic equations, which are collected into the classic compact matrix expression [32]:

$$\mathbf{A}(\omega)\mathbf{p}_s(\omega) = j\omega\rho_0\mathbf{B}(\omega)\dot{\mathbf{w}}_s(\omega) \tag{12}$$

where $\mathbf{p}_s(\omega) = \lfloor p_{s1}(\omega) \quad \cdots \quad p_{sK}(\omega)p_{sK+1}(\omega)\cdots p_{sN}(\omega)\rfloor^{\mathrm{T}}$ and $\dot{\mathbf{w}}_s = \lfloor \dot{w}_{s1}(\omega) \quad \cdots \quad \dot{w}_{sK}(\omega)0\cdots 0\rfloor^{\mathrm{T}}$ represent $N\times 1$ vectors with the complex amplitudes of respectively the pressures and velocities at the nodal points of the BEM model for the flexible box and rigid basement structure formed by the two discs. As can be noted, the vector $\dot{\mathbf{w}}_s$ encompasses $N-K$ velocities, which are set to zero in correspondence to the nodal points of the BEM model lying on the rigid basement discs and on the edges of the box. However, the sound pressures of these nodal points are not zero since they represent the discs scattered sound pressure. The vector with the unknown sound pressures on the surface of the vibrating box and on the surface of the base disks can be derived straightforwardly with the following relation:

$$\mathbf{p}_s(\omega) = \mathbf{Z}(\omega)\dot{\mathbf{w}}_s(\omega) \tag{13}$$

where

$$\mathbf{Z}(\omega) = j\omega\rho_0\mathbf{A}^{-1}(\omega)\mathbf{B}(\omega).$$

The vector with the nodal velocities was obtained from the camera measurements:

$$\dot{\mathbf{w}}_s(\omega) = j\omega\boldsymbol{\alpha}_s(\omega)f(\omega) \tag{14}$$

where the $N\times 1$ vector $\boldsymbol{\alpha}_s(\omega) = \lfloor \alpha_{s,1}(\omega) \quad \cdots \quad \alpha_{s,K}(\omega)0\cdots 0\rfloor^{\mathrm{T}}$ contains the dynamic flexibility FRFs reconstructed with Eq. (4) from the camera measurements at the first K nodal points laying on the flexible structure of the box. The values for the remaining $N-K$ points are set to 0 since they belong to the rigid basement discs and edges of the prism. More details on the derivation of the matrices $\mathbf{A}$ and $\mathbf{B}$ can be found in Ref. [32]. It is worth noting that the methodology described here remains applicable for other choices of element type or shape functions.

3.2.1. Far-field formulation

As anticipated above, in the far-field formulation, the total radiated sound power is derived by integrating the sound intensity over a large surface where the radiated sound waves locally resemble plane waves. Since the height of the box enclosure considered in this study is greater than the dimensions of its base surface, as recommended by the ISO 3744, the large cylindrical far-field measurement surface shown in Fig. 5b is adopted, which has a diameter $D_s = 2240$mm and height $H_s = 1420$mm. In general, a box-like surface that replicates the shape of the radiator would be preferred, however, as discussed in Section 2.3, a cylindrical surface has been chosen to simplify the acoustic measurements that had to be taken for the experimental validation. In this case, assuming time-harmonic acoustic waves, the total time-averaged sound power radiated by the vibrating structure can be expressed as [31]:

$$\overline{P}(\omega) = \frac{1}{2}\int_{\Omega_a} \mathscr{Re}\{p^*(\mathbf{x}_a,\omega)\dot{u}(\mathbf{x}_a,\omega)\}\mathrm{d}\Omega_a \tag{15}$$

where $p(\mathbf{x}_a,\omega)$ and $\dot{u}(\mathbf{x}_a,\omega)$ denote the complex amplitudes of the acoustic pressure and particle velocity at position $\mathbf{x}_a$ on the far field surface Ω_a enclosing the radiator. Also, $()^*$ is the complex-conjugate of the argument. Since over Ω_a the acoustic wave locally resembles a plane wave, the particle velocity is oriented normal to the surface and it is given by $\dot{u}(\mathbf{x}_a,\omega) = p(\mathbf{x}_a,\omega)/(\rho_0 c)$, where $\rho_0 c$ is the characteristic impedance given by the product of the density of air ρ_0 and the speed of sound in air c. Thus, the total sound power radiation can be expressed in terms of the following integral

$$\overline{P}(\omega) = \frac{1}{2\rho_0 c}\int_{\Omega_a} |p(\mathbf{x}_a,\omega)|^2 d\Omega_a \tag{16}$$

which can be discretized into the following midpoint Riemann sum:

$$\overline{P}(\omega) \cong \frac{1}{2\rho_0 c}\sum_{m=1}^{M}\Omega_m |p_m(\omega)|^2. \tag{17}$$

Here, following the ISO 3744 guideline, the surface Ω_a has been divided into $M = 96$ elements and $p_m(\omega)$ is the complex sound pressure at the centre of the m-th area Ω_m. The vector $\mathbf{p}_a(\omega)$ with the complex sound pressures at the centres of the 96 measurement points is derived from the BEM model using the following matrix relation that accounts for both the direct radiation and the scattering effects of the vibrating box [32]:

$$\mathbf{p}_a(\omega) = \mathbf{A}_a(\omega)\mathbf{p}_s(\omega) + j\omega\rho_0\mathbf{B}_a(\omega)\dot{\mathbf{w}}_s(\omega) \tag{18}$$

Here the matrices $\mathbf{A}_a$ and $\mathbf{B}_a$ have been derived with a procedure like that adopted for the matrices $\mathbf{A}$ and $\mathbf{B}$ in Equation (12). Also, the vectors $\mathbf{p}_s(\omega)$ and $\dot{\mathbf{w}}_s$ are derived from Eq. (12) and (13) using the dynamic flexibility FRFs obtained from the camera recordings. Overall, the derivation of the sound pressures at the far field integration positions requires a two-step procedure, where the scattered sound pressures are first derived on the surface of the box with Eq. (12) and then the pressures at the far field integration positions are derived with Eq. (18) such that:

$$\overline{P}(\omega) \cong \frac{1}{2\rho_0 c}\dot{\mathbf{w}}_s^H(\omega)\mathbf{B}_{as}^H(\omega)\Omega_a\mathbf{B}_{as}(\omega)\dot{\mathbf{w}}_s(\omega) \tag{19}$$

where $\mathbf{B}_{as}(\omega) = [\mathbf{A}_a(\omega)\mathbf{Z}(\omega) + j\omega\rho_0\mathbf{B}_a(\omega)]$ and the diagonal matrix Ω_a contains the areas Ω_m. Thus, recalling the expression for the complex velocities derived from the camera acquisitions in Eq. (14), the total sound power radiation can be derived from the following compact matrix expression:

$$\overline{P}(\omega) \cong \frac{1}{2\rho_0 c}\omega^2\boldsymbol{\alpha}_s^H(\omega)\mathbf{B}_{as}^H(\omega)\Omega_a\mathbf{B}_{as}(\omega)\boldsymbol{\alpha}_s(\omega)|f(\omega)|^2 \tag{20}$$

The total sound power radiation was also derived from the laser vibration measurements. Here, Eq. (20) was still used, except that the vector with the dynamic flexibility FRFs was built from the mobility FRFs measured with the laser vibrometer such that $\boldsymbol{\alpha}_s(\omega) = \mathbf{Y}_s(\omega)/(j\omega)$ and $\mathbf{Y}_s(\omega) = \lfloor Y_{s,1}(\omega) \quad \cdots \quad Y_{s,K}(\omega)0\cdots0\rfloor^{\mathrm{T}}$ contains the mobilities measured at the mesh of nodal points of the flexible faces and zeros at the nodal points in the rigid base discs and edges of the prism. As anticipated in Section 2.3, the measurement approach proposed in this study has been validated against classical acoustic measurement taken in an anechoic room with the array of microphones depicted in Fig. 4b. In this case the acoustic FRFs $H_m(\omega) = p_m(\omega)/f(\omega)$ were measured such that, recalling Eq. (17), the total time-averaged sound power radiated by the vibrating structure was calculated with the following formula:

$$\overline{P}(\omega) \cong \frac{1}{2\rho_0 c}\mathbf{H}_{af}^H(\omega)\Omega_a\mathbf{H}_{af}(\omega)|f(\omega)|^2 \tag{21}$$

where the vector $\mathbf{H}_{af}(\omega) = \lfloor H_1(\omega) \quad \cdots \quad H_m(\omega)\rfloor^{\mathrm{T}}$ contains the M FRFs $H_m(\omega) = p_m(\omega)/f(\omega)$ measured at the grid of points depicted in Fig. 4a with the microphones array depicted in Fig. 4b.

3.2.2. Near-field formulation

As shown in Fig. 5a, in the near-field formulation, the total radiated sound power is derived by integrating the sound intensity over the surface of the radiator itself. This is quite a convenient solution since it relies on the vibration velocities reconstructed from the camera measurements and sound pressure derived from the first step of the BEM formulation presented above, which also depends on the velocities reconstructed from the camera measurements. Indeed, the sound radiation is derived directly from the vibration velocities on the boundary surface of the radiator, thus exploiting the high-density grid of points provided by the Digital Image Correlation (DIC) surface tracking. Conversely, evaluating the sound power in the far-field requires a subsequent, second BEM step to numerically propagate the acoustic quantities from the boundary surface to an external far-field mesh. Replicating the same high spatial resolution (the same large quantity of points) on that external far-field surface would make this second BEM propagation step particularly cumbersome and computationally expensive. By stopping at the first step, the near-field approach preserves the full spatial richness of the optical measurement while avoiding a highly onerous second calculation phase. Thus, in this case, since the integration surface in Eq. (15) coincides with the surface of the box, i.e. $\Omega_a \equiv \Omega_s$, the acoustic particle velocity coincides with the vibration velocity of the box. Hence, the total sound power radiation given in Eq. (15) becomes [31]:

$$\overline{P}(\omega) = \frac{1}{2}\int_{\Omega_s} \mathscr{Re}\{p^*(\mathbf{x}_s,\omega)\dot{w}(\mathbf{x}_s,\omega)\}\mathrm{d}\Omega_s \tag{22}$$

This integral can be broken into a summation of N_e integrals over the areas of the triangular elements of the BEM model, such that, recalling Eqs. (8) and (9), it results

$$\overline{P}(\omega) \cong \frac{1}{2}\sum_{e=1}^{N_e}\mathscr{Re}\left\{\mathbf{p}_{se}^{\mathrm{H}}(\omega)\mathbf{C}_e\dot{\mathbf{w}}_{se}(\omega)\right\} \tag{23}$$

where

$$\mathbf{C}_e = \int_{A_e} \mathbf{N}^{\mathrm{T}}(\xi,\eta)\mathbf{N}(\xi,\eta)\det(\mathbf{J}_e)\mathrm{d}A_e \tag{24}$$

and $\mathbf{J}_e$ is the Jacobian. Here the integration was performed with Gaussian quadrature. Equation (24) can be rewritten in the following compact form:

$$\overline{P}(\omega) \cong \frac{1}{2}\mathscr{Re}\left\{\mathbf{p}_s^{\mathrm{H}}(\omega)\mathbf{C}\dot{\mathbf{w}}_s(\omega)\right\} \tag{25}$$

where the $\mathbf{C}$ matrix is built by properly assembling in the relevant rows and columns the elements of the matrices $\mathbf{C}_e$ of all elements. Recalling Equation (13), the total sound power radiation becomes:

$$\overline{P}(\omega) \cong \frac{1}{2}\mathscr{Re}\left\{\dot{\mathbf{w}}_s^{\mathrm{H}}(\omega)\mathbf{Z}^{\mathrm{H}}(\omega)\mathbf{C}\dot{\mathbf{w}}_s(\omega)\right\} \tag{26}$$

Finally, if the matrix $\mathbf{Z}^{\mathrm{H}}(\omega)\mathbf{C}$ is symmetric, the radiated power reduces to the classical form involving the radiation resistance matrix $\mathbf{R}(\omega) = \frac{1}{2}\mathscr{Re}\left\{\mathbf{Z}^{\mathrm{H}}(\omega)\mathbf{C}\right\}$:

$$\overline{P}(\omega) \cong \dot{\mathbf{w}}_s^{\mathrm{H}}(\omega)\mathbf{R}(\omega)\dot{\mathbf{w}}_s(\omega) \tag{27}$$

As seen above the total radiated sound power can thus be expressed with respect to the dynamic flexibility FRFs reconstructed from the camera measurements or the mobility FRFs measured with the laser vibrometer such that:

$$\overline{P}(\omega) \cong \omega^2\boldsymbol{\alpha}_s^H(\omega)\mathbf{R}(\omega)\boldsymbol{\alpha}_s(\omega)|f(\omega)|^2 \tag{28}$$

Equation (27) presents quite an important expression since, as shown in [32], with a proper eigenvalue–eigenvector decomposition it can be conveniently reformulated in terms of the so called "vibration modes", which provide an effective means to represent the physics of the sound radiation. The reader interested into the details of this technique is referred to Ch. 3.7 of Ref. [32].

3.3. Calculation of SWL third octave band spectrum

The third octave band spectrum of the radiated sound power level was obtained from the frequency-dependent radiated sound power $\overline{P}(\omega)$ using the following relations for the n-th band [19]:

$$SWL_{\mathrm{n}} = 10\log_{10}\frac{\overline{P}_{\mathrm{n}}}{P_{\mathrm{r}}} \tag{29}$$

Here $P_{\mathrm{r}} = 10^{-12}$W is the reference value for sound power and the band-limited values $\overline{P}_{\mathrm{n}}$ are given by:

$$\overline{P}_{\mathrm{n}} = \sum_{j=j_1}^{j_2}\frac{\Delta B_{\mathrm{n}}}{N_{\mathrm{j}}}\overline{P}(\omega_j)\left|f(\omega_j)\right|^2 \tag{30}$$

where ΔB_{n} is the width of the n-th third-octave band and $N_{\mathrm{j}} = j_2 - j_1$, where j_1, j_2 are the indices of the frequency-samples at the lower and maximum frequency of the third-octave band [2].

It is important to emphasise that, to allow accurate comparisons of the camera-based measurement of the vibration and sound radiation spectra and the direct measurements with the spectra measured with the laser vibrometer and microphone array, the formulations presented in this paper refer to the force exerted by the shaker. In practical applications where the vibration of the box is generated by the machinery encased in the enclosure there is no access to a reference signal for the excitation. In this case, rather than considering the dynamic flexibility FRFs reconstructed from the camera acquisitions, the raw spectra of the vibrations reconstructed from the camera acquisitions should be used instead.

4. Measurement results

The practical implementation of the approach proposed in this paper for the measurement of the narrow and third octave band spectra of the sound radiation by vibrating bodies using optical camera recordings is now discussed for the box model structure described in Section 2.1 and depicted in Fig. 1. To start with, the narrow band spectrum of the total flexural kinetic energy derived from the camera recordings using the formulation presented in Section 3.1 are analysed and contrasted with that obtained from the laser vibrometer acquisitions. The analysis is limited to 2 kHz. This limit depends on few factors, such as the measurement equipment (i.e. the camera), the measurement methodology (i.e. the mathematical formulation and algorithms) and the type (i.e. tonal, broadband, transient, etc.) and level of vibration of the machinery/structure being tested. It is worth stressing that a fixed upper measurement cut-off frequency cannot be universally defined for the methodology presented in this paper, as the frequency limit depends directly on the optical Signal-to-Noise Ratio (SNR) relative to the physical displacement amplitudes of the analysed structure. Therefore, the applicable frequency range is highly case-dependent, governed by the specific structural dynamics and the localization of resonance frequencies relative to the camera tracking capability, beyond which optical noise begins to dominate. The flexural deflection shapes at the principal resonance frequencies are also reported to provide a physical understanding of the flexural response of the box. Then, the narrow and third octave band spectra of the total radiated sound power derived with the far field and near field formulations presented in Sections Sections 3.2.1 and 3.2.2 are thoroughly investigated and compared with those obtained from the classical acoustic measurements implemented in the semi-anechoic room according to the ISO 3744:2026.

4.1. Camera versus laser vibrometer vibration measurement

Fig. 6 shows the spectra of the time-averaged total flexural kinetic energy per unit force excitation of the box structure obtained with Equation (7) using the high-speed camera measurements (in red) and with Equation (8) using the laser vibrometer measurements (in blue). The two spectra overlap rather well. They show several well-defined resonance peaks, indicating that, in this frequency band, the flexural response is characterised by a relatively low modal overlap [75]. In general, compared to the spectrum derived from the laser vibrometer measurements, the spectrum reconstructed from the camera measurements is characterised by less pronounced resonance peaks. This is primarily due to the fact that the spectrum obtained from the camera recordings was reconstructed with a coarser frequency sampling than the spectrum obtained from the laser vibrometer measurements. To better interpret these deviations, the camera measurement error budget was considered, which accounts for uncertainty sources in both the image-based displacement identification and spatial reconstruction stages. For the Photron FASTCAM SA-Z system with DIC and ArUco-based calibration, primary contributions arise from subpixel displacement resolution limits (down to 10^{-3} pixel), speckle pattern quality, DIC subset size, and interpolation bias. Comprehensive guidelines for such DIC uncertainty quantifications are provided by Peshave *et al.* [76], while the subpixel resolution limits for optical-flow-based methods are established by Javh *et al.* [77]. Also, at higher frequencies above 1750 Hz, the camera-based spectrum exhibits an increased level of noise, which can be attributed to two concurrent factors: on the one hand, as the structural displacement drops near the camera noise floor under low signal-to-noise ratio (SNR) conditions, the combined effect of the subpixel resolution limit and the temporal noise floor restricts the optimal usable range up to 1750 Hz. Since the reconstructed flexural vibration kinetic energy depends on the integration of squared surface vibration velocities, this background noise artificially inflates the estimated structural response. On the other hand, the frequency-domain triangulation introduces geometric errors from perspective scale-factor approximation, following the framework of Gorjup *et al.* [78]. While absolute calibration errors affect the static geometry reconstruction, for small vibrations, they are less relevant in relative displacement measurements [79]; however, in the high-frequency range, this linear

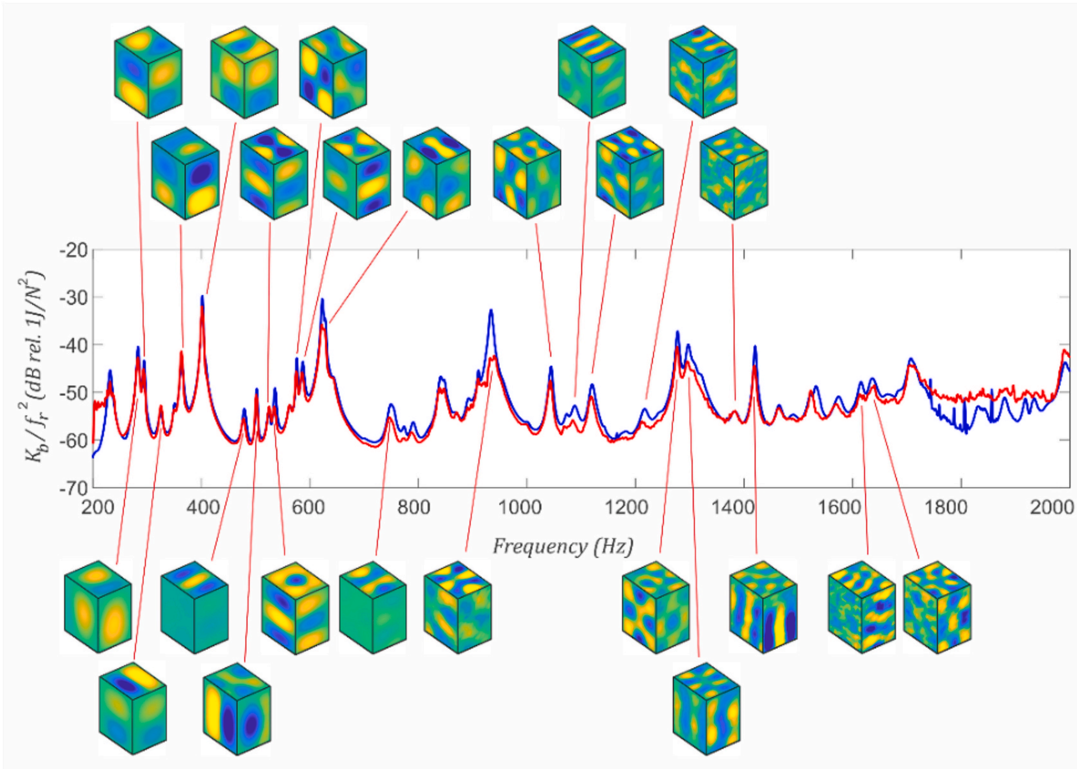

Fig. 6. Narrow band spectra of the total vibration kinetic energy per unit force excitation from measurements with laser vibrometer (blue line) and camera (red line) with principal deflection shapes obtained from camera measurements.

triangulation of frequency-domain image data does not allow an accurate estimate of the Fourier transforms necessary to derive the dynamic stiffness FRFs defined in Eq. (4). Most likely, the combination of these two aspects has led to the noisy spectrum visible above 1750 Hz.

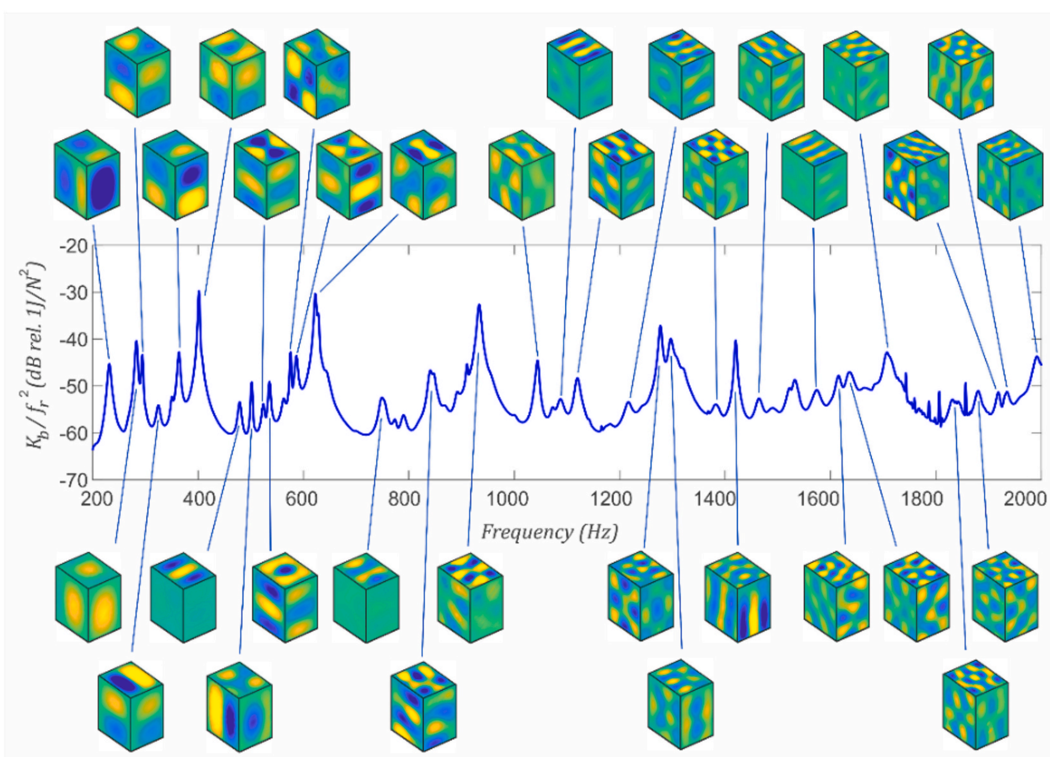

Fig. 7. Narrow band spectrum of the total vibration kinetic energy per unit force excitation from measurements with laser vibrometer (blue line) with principal deflection shapes obtained from laser vibrometer measurements.

The insets in Fig. 6 show the deflection shapes of the box derived from the dynamic stiffness FRFs reconstructed from the camera recordings at the most relevant resonance frequencies. In general, each face is characterised by the typical deflection shapes of constrained rectangular panels with the distinctive lobes characterised by the mode orders n_1, n_2. However, there are some resonance frequencies where the vibration is restricted on a specific face. For example, the resonance at 750 Hz is dictated by a resonance effect localised on the top face. Comparing these deflection shapes with those depicted in Fig. 7, which were derived from the mobility FRFs measured with the laser vibrometer, a good agreement is observed. This confirms that the camera-based vibration measurement approach accurately reconstructs the whole vibration field of the box and thus should provide a good basis for the derivation of the sound radiation.

4.2. SWL far-field approach

The reconstruction of the total sound power radiation from the camera measurements is now discussed and contrasted with that obtained from the laser vibrometer measurements and the sound power measurements in the semi-anechoic room with the microphones array. To start, the spectra of the total sound power radiation derived using the far field formulation presented in Section 3.2.1 are considered. The red line in Fig. 8 shows the narrow-band spectrum obtained from the camera measurements with Eq. (20), whereas the blue line in Fig. 9 depicts the narrow-band spectrum derived from the laser vibrometer measurements with Eq. (20) setting $\boldsymbol{\alpha}_s(\omega) = \mathbf{Y}_s(\omega)/(j\omega)$. The black lines in both graphs show the reference narrow band spectrum obtained from the microphone measurements with Eq. (21).

In general, both the narrow-band spectrum reconstructed from the camera measurements and that reconstructed from the laser vibrometer agree well with that obtained from the direct acoustic measurements in the semi-anechoic room. As found for the vibration spectrum of the total flexural kinetic energy shown in Fig. 6, these spectra are characterised by sharp resonance peaks at the resonance frequencies of the box structure although, here the amplitudes of the peaks do not match those found in the vibration spectrum. This is due to the fact that, at resonance frequency, the flexural response is controlled by a specific resonant mode whose sound radiation efficiency depends on the shape of the mode itself. For instance, as discussed in Ref. [32], in general, odd mode orders are better radiators that even mode orders. For example, the (1,1) mode radiates sound more efficiently than the (2,1), (1,2), (2,2) modes, which are characterised by a sort of natural cancellation of the sound radiation produced by the anti-phase vibration of the lobes. The spectrum reconstructed from the camera measurements (red line) is slightly noisier than both that derived from the laser vibrometer measurements (blue line) and that obtained from the acoustic measurements in the semi-anechoic room (black line). Moreover, as already seen for the vibration spectrum, it is significantly noisier at frequencies above 1750 Hz. As discussed above these noise problems depends on both the low amplitude of the measured vibrations and the frequency triangulation used to reconstruct the displacements, which concur to generate noisy Fourier transforms for the frequency domain triangulation described in Section 3.1.

Considering now the third octave band spectra of the sound power levels (SWL) shown in Fig. 10, a close agreement is found between the spectra obtained from the camera measurements (red bars), the laser vibrometer measurement (blue bars) and the acoustic measurements in the semi-anechoic room (black bars). Indeed, deviations comprised between 0 and 3 dB are found between the three measurements, which is a rather good result, particularly in view of the fact that the reference acoustic measurement taken into the anechoic room according to the ISO 3744:2026 standard are of engineering accuracy and may have been affected by flanking noise and other features of the measurement setup too.

To provide a more rigorous validation beyond the visual overlap of the curves, the discrepancies in the reconstructed Total Sound Power radiation and the SWL have been quantified using the Mean Absolute Error ΔSWL expressed in decibels (dB). Specifically, three distinct error metrics have been defined to evaluate the deviations between the LDV and the microphone array ($\Delta SWL_{v,m}$), between the proposed camera approach and the standardized microphone array ($\Delta SWL_{c,m}$), and between the LDV-based acoustic prediction and the camera-approach ($\Delta SWL_{v,c}$):

$$\begin{cases} \Delta SWL_{v,m} = \dfrac{1}{N}\sum_{i=1}^{N} |SWL_v - SWL_m| \\ \Delta SWL_{c,m} = \dfrac{1}{N}\sum_{i=1}^{N} |SWL_c - SWL_m| \\ \Delta SWL_{v,c} = \dfrac{1}{N}\sum_{i=1}^{N} |SWL_v - SWL_c| \end{cases} \tag{31}$$

where N represents the number of considered third-octave bands or sampled frequencies. The computed far-field quantitative metrics are summarized in Table 2. For the narrow-band spectrum, the error of the camera approach aligns closely with the baseline experimental discrepancy observed between the other two methods. When moving to the third-octave band resolution, the errors decrease consistently across all comparisons. These low values provide practical evidence of accuracy within the tested conditions. Here it should be recalled that the reference ISO 3744 (grade 2) measurement approach is also affected by uncertainty. Thus, the errors reported in Table 2 may be overestimated.

4.3. SWL near-field approach

The spectra of the total sound power radiation derived using the near field formulation presented in Section 3.2.2 are now examined. Here, the same layout of the plots presented in the previous section is used such that the red, blue and black lines in Figs. 11 and 12 show respectively the narrow-band spectra obtained from the camera measurements

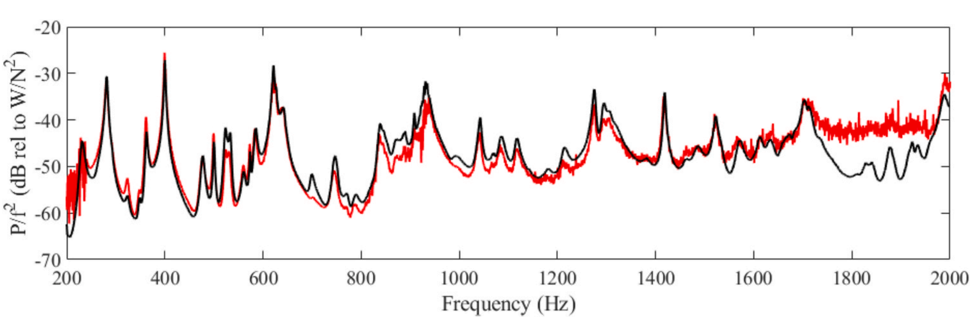

Fig. 8. Narrow band spectra of the total sound power radiation per unit force excitation from measurements with microphones (black line) and reconstructed at microphones from measurements with camera – far-field approach (red line).

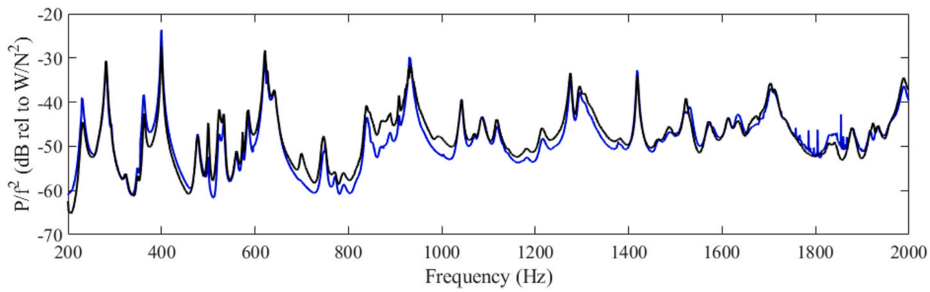

Fig. 9. Narrow band spectra of the total sound power radiation per unit force excitation from measurements with microphones (black line) and reconstructed at microphones from measurements with laser vibrometer – far-field approach (blue line).

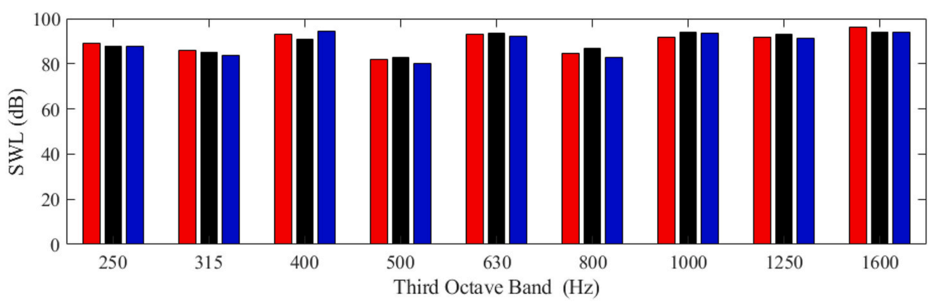

Fig. 10. Third-octave band spectra of the total sound power levels from measurements with microphones (black bars) and reconstructed at microphones positions from measurements with laser vibrometer (blue bars) and camera – far-field approach (red bars) –.$\mathrm{dB\,rel.\,to\,}10^{-12}\,\mathrm{W}$

Table 2
Quantitative mean absolute errors for the far field approach.

		$\Delta SWL_{v,m}$(dB)	$\Delta SWL_{c,m}$(dB)	$\Delta SWL_{v,c}$(dB)
Far Field	Narrow band	1,8	2,6	2,2
	Third-octave band	1,7	1,4	1,5

with Eq. (28), the laser vibrometer measurements with Eq. (28) setting $\boldsymbol{\alpha}_s(\omega) = \mathbf{Y}_s(\omega)/(j\omega)$ and the microphone measurements with Eq. (21).

Yet again the two narrow-band spectra reconstructed from the camera measurements and that reconstructed from the laser vibrometer match well with that obtained from the direct acoustic measurements in the semi-anechoic room. Again, the spectrum reconstructed from the camera measurements (red line) is noisier than both that derived from

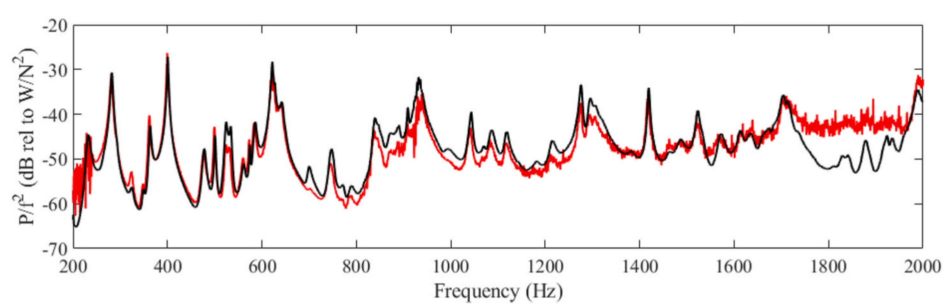

Fig. 11. Narrow band spectra of the total sound power radiation per unit force excitation from measurements with microphones (black line) and calculated from measurements with camera – near-field approach (red line).

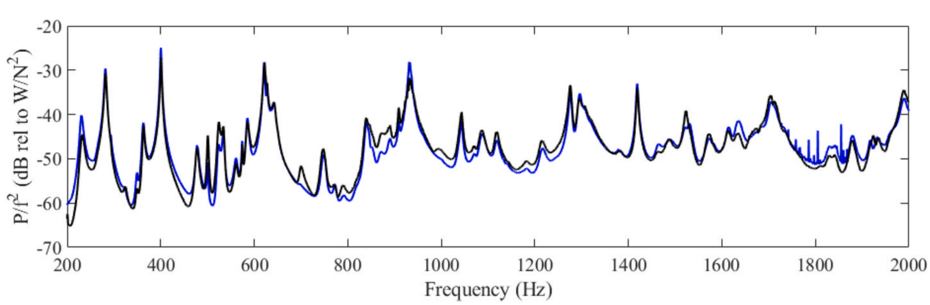

Fig. 12. Narrow band spectra of the total sound power radiation per unit force excitation from measurements with microphones (black line) and calculated from measurements with laser vibrometer – near-field approach (blue line).

the laser vibrometer measurements (blue line) and that obtained from the acoustic measurements in the anechoic room (black line), in particular above 1750 Hz.

The third octave band spectra of the sound power level (SWL) in Fig. 13, show that, with the nearfield formulation, the spectra obtained from the camera measurements (red bars) and the laser vibrometer measurement (blue bars) are characterised by deviations comprised between 0 and 2 dB with respect to that obtained from the acoustic measurements in the anechoic room (black bars), which, as discussed above, are of engineering accuracy and may have been affected by flanking noise and other features of the measurement setup. Overall, compared to the far-field method, the near-field approach provides a more accurate measurement and this may be the result of the fact that, here, the total sound power radiation is derived from the summation of the sound intensity over the dense grid of nodal points of the BEM model rather than the coarser grid of points defined in the far-field surface. To be fair, it should be highlighted that in the far-field the acoustic wavefronts have flattened and thus, compared to the near-field, the derivation of the total sound power radiation may require a coarser grid of points. Nevertheless, the results in Figs. 10–13 seem to indicate that the SWLs derived with the near-field formulation are more accurate than those obtained with the far-field approach.

Here too, to provide a more rigorous validation beyond the visual overlap of the curves, the discrepancies in the reconstructed Total Sound Power radiation and the SWL have been quantified using the Mean Absolute Error expressed in decibels (dB) according to Eq. (31). The computed near-field quantitative metrics are summarized in Table 3. For the narrow-band spectrum, the error of the camera approach aligns closely with the baseline experimental discrepancy observed between the two traditional sensors. When moving to the third-octave band resolution, the errors decrease consistently across all comparisons. These low values confirm that the proposed optical methodology maintains a high global accuracy within the tested conditions, providing a robust and statistically sound alternative to traditional acoustic testing. As seen above, it is important to consider that the ISO 3744 (grade 2) acoustic measurements also affected by uncertainty and thus the errors reported in Table 3 may be overestimated.

For completeness, the A-weighted total radiated sound power level was also calculated over the frequency range covered by the 250 Hz to 1600 Hz third octave bands. The value obtained from microphone measurements is 87 dBA, while the total radiated power derived from camera measurements is 86.6 dBA, and that obtained from laser vibrometer data is 86.9 dBA.

5. Conclusions

This study has presented an additional methodology for the measurement of the narrow band and third octave band spectra of the total sound power radiation by vibrating bodies, which has been tested on a thin-walled box model structure. The approach is based on a core matrix formulation that integrates over the surface of the radiator the flexural vibration field reconstructed from multi-view recordings taken with a high-speed optical camera and the radiation resistance matrix derived with a boundary element model. A finite element model with infinite free field or other non-reflecting boundary elements could be used too.

The narrow band spectra of the time-averaged total flexural kinetic energy and time-averaged total radiated sound power derived from the multi-view camera acquisitions have been validated against the equivalent spectra derived from measurements taken with a laser vibrometer and a microphone setup arranged in a semi-anechoic room according to the ISO 3744:2026 guidelines. In general, the narrow band spectra derived from the multi-view camera acquisitions overlap well with the spectra reconstructed from the laser vibrometer and the acoustic measurements. However, they show less pronounced resonance peaks due to the coarser frequency sampling obtained from the frequency triangulation of the camera recordings. Also, above 1750 Hz they are rather noisy due to the concurrent effects of low amplitude vibration measurements and poor reconstruction of the spectra with the frequency triangulation of the camera recordings. Overall, these tests confirm the validity of the proposed measurement approach and suggest that cameras with both very high spatial resolution and very high acquisition time-rates should be employed to accurately reconstruct the vibration and sound radiation spectra in audio frequency ranges of typical machineries.

The third octave band spectrum of the radiated sound power level (SWL) derived from the multi-view camera acquisitions has also been reconstructed and validated against the equivalent spectrum derived from acoustic measurements taken in the semi-anechoic room according to the ISO 3744:2026 guidelines. Here too, a good agreement has been found with deviations comprised between 0 and 2 dB.

Besides the near-field formulation where the radiation sound power is derived directly on the surface of the radiator, a far-field formulation has also been considered in this study, which nevertheless involves more computation steps and has proven slightly less accurate with deviations comprised between 0 and 3 dB between the third octave band spectrum obtained from the camera measurements and that derived from the acoustic measurements. This is due to the fact that, in this case, the sound power radiation has been derived with a coarser quadrature over the large far-field surface. Here, the A-weighted total radiated sound power levels were also calculated over the frequency range of the 250–1600 Hz third octave bands. Compared to the 87 dBA reference value obtained from microphone measurements, the values derived from the camera and laser vibrometry measurements show very small deviations of −0.4 dBA and −0.1 dBA respectively.

Overall, the study demonstrates that high-speed camera

Table 3
Quantitative mean absolute errors for the near field approach.

		$\Delta SWL_{v,m}$(dB)	$\Delta SWL_{c,m}$(dB)	$\Delta SWL_{v,c}$(dB)
Near Field	Narrow band	1,4	2,6	1,9
	Third-octave band	1,2	1,4	0,9

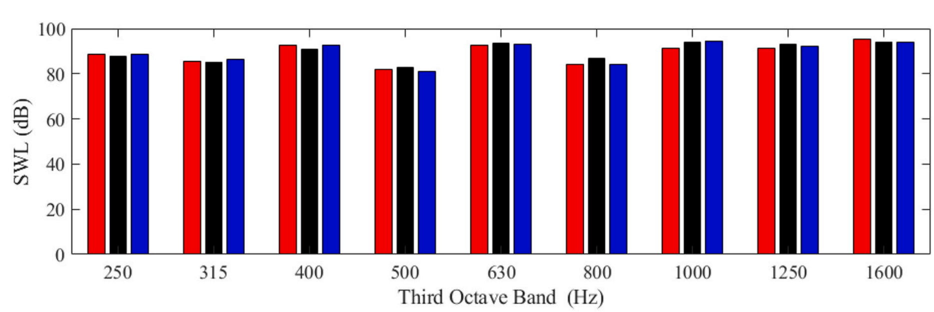

Fig. 13. Third-octave band spectra of the total sound power levels from measurements with microphones (black bars) and calculated from measurements with laser vibrometer (blue bars) and camera – near-field approach (red bars) –.dB ref. 10^{-12}

measurements combined with BEM (or FEM) models of the radiator can be effectively used to reconstruct the total flexural vibration and total sound power radiation of practical machinery characterised by bodies with complex shapes. In particular, it relies on short-time full-field video acquisitions, performed in-situ such that the effects due to variability of measurement conditions are minimised and there is no need to move the machine into classical acoustic measurement facilities. Moreover, it can be used to investigate the physics of the structure-borne sound radiation. In particular, the sound radiation of specific portions of the body can be distinguished. Moreover, radiation modes of the whole structure can be reconstructed straightforwardly with an eigenvalue–eigenvector decomposition that provides an indication of how the vibration response should be tailored to reduce the sound radiation. Finally, the sound radiation into virtual environments could also be simulated and used to choose where to install the machinery and to design appropriate sound absorption/insulation treatments.

However, it should be highlighted that, in general, the proposed method will be limited to frequency ranges in which the available camera, i.e., their spatial and temporal resolution, allows the reconstruction of the vibration displacement field, whose amplitude generally decreases with increasing frequency for typical structures. Also, it is expected that the reconstruction of the vibration field, and thus of the sound radiation, will be rather challenging in presence of structures or bodies having complex geometries involving obstructed surfaces, cables, coatings, etc. Finally, applying a speckle pattern to the radiating surfaces may be a labor-intensive process, and the coating itself may alter the vibration response of thin, lightweight structures.

CRediT authorship contribution statement

Sofia Baldini: Writing – original draft, Validation, Methodology, Investigation, Formal analysis, Conceptualization. **Elke Deckers:** Writing – original draft, Validation, Methodology, Investigation, Formal analysis, Conceptualization. **Hervè Denayer:** Writing – original draft, Validation, Methodology, Investigation, Formal analysis, Conceptualization. **Luyao Dong:** Writing – original draft, Validation, Methodology, Investigation, Formal analysis, Conceptualization. **Paolo Gardonio:** Writing – original draft, Validation, Methodology, Investigation, Formal analysis, Conceptualization. **Domen Gorjup:** Writing – original draft, Validation, Methodology, Investigation, Formal analysis, Conceptualization. **Dionysios Panagiotopoulos:** Writing – original draft, Validation, Methodology, Investigation, Formal analysis, Conceptualization. **Roberto Rinaldo:** Writing – original draft, Validation, Methodology, Investigation, Formal analysis, Conceptualization. **Janko Slavič:** Writing – original draft, Validation, Methodology, Investigation, Formal analysis, Conceptualization.

Declaration of competing interest

The authors declare that they have no known competing financial interests or personal relationships that could have appeared to influence the work reported in this paper.

Acknowledgements

The authors would like to acknowledge the ESPERT project, which was supported by the University of Udine Research Programme and the partial financial support from the Slovenian Research Agency, Slovenia (research core funding No. P2-0263). The research of L. Dong was funded by a grant within the European Marie Sklodowska Curie Action Doctoral Network (GA 101073014). Views and opinions expressed are however those of the authors only and do not necessarily reflect those of the European Union. The European Union cannot be held responsible for them. Internal Funds KU Leuven are gratefully acknowledged for their support.

Data availability

Data will be made available on request.

References

[1] R.F. Barron, Industrial noise control and acoustics, Marcel Dekker Inc., New York, 2003.
[2] D.A. Bies, C.H. Hansen, Engineering noise control : theory and practice, Crc Press, 2017.
[3] F. Pedrielli, E. Carletti, The revision of the directive 2000/14/EC: a never ending story, in: Proceedings of the 10th Convention of the European Acoustics Association Forum Acusticum 2023, European Acoustics Association, Turin, Italy, 2024, pp. 1419–1425, https://doi.org/10.61782/fa.2023.0075.
[4] C.S. Hayden, E.L. Zechmann, Estimation of sound pressure level exposures from sound power level measurements of powered hand-tools, Noise Control Eng. J. 55 (4) (2007) 379, https://doi.org/10.3397/1.2750437.
[5] X.F. Wang, J. Shi, The powertrain in vehicle sound power test method research, Appl. Mech. Mater. 380–384 (2013) 77–81, https://doi.org/10.4028/www.scientific.net/AMM.380-384.77.
[6] L. Fredianelli, M. Nastasi, M. Bernardini, F. Fidecaro, G. Licitra, Pass-by characterization of noise emitted by different categories of seagoing ships in ports, Sustainability 12 (5) (2020) 1740, https://doi.org/10.3390/su12051740.
[7] Y.Z. Zhao, S.X. Wu, J.Z. Qiu, L.L. Wu, H. Huang, Sound power level measurement of sheng, a Chinese wind instrument, J. Acoust. Soc. Am. 123 (5_Supplement) (2008) 3240, https://doi.org/10.1121/1.2933489.
[8] ISO (International Organization for Standardization), 2025, "ISO 3744:2025: Acoustics - Determination of Sound Power Levels and Sound Energy Levels of Noise Sources Using Sound Pressure - Engineering Methods for an Essentially Free Field over a Reflecting Plane".
[9] F. Heisterkamp, J. Schmitt, J. Hook, Simplification of ISO 3744 - making the most important standard for determination of sound power levels easier to use, in: INTER-NOISE and NOISE-CON Congress and Conference Proceedings, 2023, pp. 319–326, https://doi.org/10.3397/IN_2022_0049.
[10] ISO (International Organization for Standardization), 2010, "ISO 3741:2010: Acoustics — Determination of Sound Power Levels and Sound Energy Levels of Noise Sources Using Sound Pressure — Precision Methods for Reverberation Test Rooms".
[11] ISO (International Organization for Standardization), 2017, "ISO 3745:2012+A1: 2017: Acoustics - Determination of Sound Power Levels and Sound Intensity Levels of Noise Sources Using Sound Pressure - Precision Methods for Anechoic Rooms and Hemi-Anechoic Rooms".
[12] ISO (International Organization for Standardization), 2012, "ISO 3745:2012: Acoustics — Determination of Sound Power Levels and Sound Energy Levels of Noise Sources Using Sound Pressure — Precision Methods for Anechoic Rooms and Hemi-Anechoic Rooms".
[13] F. Fahy, Sound intensity, CRC Press, 1995.
[14] F. Jacobsen, H.-E. de Bree, A comparison of two different sound intensity measurement principles, J. Acoust. Soc. Am. 66 (2017) 1510–1517.
[15] J. Billingsley, R. Kinns, The acoustic telescope, J. Sound Vib. 48 (1976) 485–510.
[16] R. Merino-Martínez, P. Sijtsma, M. Snellen, T. Ahlefeldt, J. Antoni, C.J. Bahr, D. Blacodon, D. Ernst, A. Finez, S. Funke, T.F. Geyer, S. Haxter, G. Herold, X. Huang, W.M. Humphreys, Q. Leclère, A. Malgoezar, U. Michel, T. Padois, A. Pereira, C. Picard, E. Sarradj, H. Siller, D.G. Simons, C. Spehr, A review of acoustic imaging methods using phased microphone arrays, CEAS Aeronaut. J. 10 (1) (2019) 197–230, https://doi.org/10.1007/s13272-019-00383-4.
[17] G.H. Koopmann, J.B. Fahnline, Designing quiet structures. A Sound Power Minimization Approach, Academic Press, 1997.
[18] T. Padois, J. Fischer, C. Doolan, O. Doutres, Acoustic imaging with conventional frequency domain beamforming and generalized cross correlation: a comparison study, Appl. Acoust. 177 (2021) 107914, https://doi.org/10.1016/j.apacoust.2021.107914.
[19] F. Fahy, Measurement of audio-frequency sound in air, in: fundamentals of sound and vibration, CRC Press, 2015.
[20] J. Rohlfing, P. Gardonio, D.J. Thompson, Comparison of decentralized velocity feedback control for thin homogeneous and stiff sandwich panels using electrodynamic proof-mass actuators, J. Sound Vib. 330 (5) (2011) 843–867, https://doi.org/10.1016/j.jsv.2010.09.013.
[21] C.B. Jones, C.B. Goates, J.D. Blotter, S.D. Sommerfeldt, Experimental validation of determining sound power using acoustic radiation modes and a laser vibrometer, Appl. Acoust. 164 (2020) 107254, https://doi.org/10.1016/j.apacoust.2020.107254.
[22] I.C. Bacon, S.D. Sommerfeldt, J.D. Blotter, Developing an indirect vibration-based sound power method to determine the sound power radiated from acoustic sources, (2022), 065003. doi: 10.1121/2.0001732.
[23] A. Wurzinger, F. Kraxberger, P. Maurerlehner, B. Mayr-Mittermüller, P. Rucz, H. Sima, M. Kaltenbacher, S. Schoder, Experimental prediction method of free-field sound emissions using the boundary element method and laser scanning vibrometry, Acoustics 6 (1) (2024) 65–82, https://doi.org/10.3390/acoustics6010004.
[24] A. Wurzinger, S. Schoder, Uncertainty propagation for vibrometry-based acoustic predictions using Gaussian process regression, Appl. Sci. 15 (19) (2025) 10652, https://doi.org/10.3390/app151910652.

[25] ISO (International Organization for Standardization), 2009, "ISO/TS 7849-2:2009 Acoustics — Determination of Airborne Sound Power Levels Emitted by Machinery Using Vibration Measurement Part 2: Engineering Method Including Determination of the Adequate Radiation Factor".
[26] ISO (International Organization for Standardization), 2009, "ISO/TS 7849-1:2009 Acoustics — Determination of Airborne Sound Power Levels Emitted by Machinery Using Vibration Measurement. Part 1: Survey Method Using a Fixed Radiation Factor".
[27] S.J. Rothberg, M.S. Allen, P. Castellini, D. Di Maio, J.J.J. Dirckx, D.J. Ewins, B. J. Halkon, P. Muyshondt, N. Paone, T. Ryan, H. Steger, E.P. Tomasini, S. Vanlanduit, J.F. Vignola, An international review of laser doppler vibrometry: making light work of vibration measurement, Opt. Lasers Eng. 99 (2017) 11–22, https://doi.org/10.1016/j.optlaseng.2016.10.023.
[28] P. Gardonio, G. Guernieri, E. Turco, L.D. Bo, R. Rinaldo, A. Fusiello, Reconstruction of the sound radiation field from flexural vibration measurements with multiple cameras, Mech. Syst. Signal Process. 195 (2023) 110289, https://doi.org/10.1016/j.ymssp.2023.110289.
[29] S. Baldini, G. Guernieri, D. Gorjup, P. Gardonio, J. Slavič, R. Rinaldo, 3D sound radiation reconstruction from camera measurements, Mech. Syst. Signal Process. 227 (2025), https://doi.org/10.1016/j.ymssp.2025.112400.
[30] P. Gardonio, R. Rinaldo, L. Dal Bo, R. Del Sal, E. Turco, A. Fusiello, Free-field sound radiation measurement with multiple synchronous cameras, Measurement 188 (2022) 110605, https://doi.org/10.1016/j.measurement.2021.110605.
[31] P. Gardonio, S. Baldini, D. Gorjup, J. Slavič, R. Rinaldo, Narrow and third-octave spectra of total flexural vibration and sound power radiation from optical camera measurements, Mech. Syst. Signal Process. 249 (2026) 114054, https://doi.org/10.1016/j.ymssp.2026.114054.
[32] F.J. Fahy, P. Gardonio, Sound and structural vibration, Elsevier, 2007.
[33] A.D. Pierce, Acoustics, Acoustical Society of America through the American Institute of Physics, (1991).
[34] M.C. Junger, D. Feit, Sound, structures, and their interaction, The Mit Press, Imp., 2010.
[35] C. Lesuer, M. Gotteland, Rayonnement Acoustique. Éléments de Base, Rayonnement Acoustique Des Structures, y C. Lesueur Editions Eyrolles, (1988), p. Ch 3.
[36] T.C. Chu, W.F. Ranson, M.A. Sutton, Applications of digital-image-correlation techniques to experimental mechanics, Exp. Mech. 25 (3) (1985) 232–244, https://doi.org/10.1007/BF02325092.
[37] T.G. Ryall, C.S. Fraser, Determination of Structural modes of vibration using digital, J. Aircraft 39 (1) (2002) 114–119.
[38] S.W. Park, H.S. Park, J.H. Kim, H. Adeli, 3D displacement measurement model for health monitoring of structures using a motion capture system, Measurement 59 (2015) 352–362.
[39] J. Baqersad, C. Niezrecki, P. Avitabile, Full-field dynamic strain prediction on a wind turbine using displacements of optical targets measured by stereophotogrammetry, Mech. Syst. Signal Pr. 62–63 (2015) 284–295.
[40] P. Poozesh, J. Baqersad, C. Niezrecki, P. Avitabile, E. Harvey, R. Yarala, Large-area photogrammetry based testing of wind turbine blades, Mech. Syst. Signal Pr. 86B (2017) 98–115.
[41] J. Baqersad, P. Poozesh, C. Niezrecki, P. Avitabile, Photogrammetry and optical methods in structural dynamics – a, Mech. Syst. Signal Pr. 86 (2017) 17–34.
[42] R.S. Pappa, J.T. Black, J.R. Blandino, T.W. Jones, P.M. Danehy, A.A. Dorrington, Dot-projection photogrammetry and videogrammetry of gossamer space, J. Spacecraft Rockets 40 (6) (2003) 858–867.
[43] M.N. Helfrick, C. Niezrecki, P. Avitabile, T. Schmidt, 3D digital image correlation methods for full-field vibration, Mech. Syst. Signal Pr. 25 (3) (2011) 917–927.
[44] P. Reu, Introduction to digital image correlation: best practices and applications, Exp. Tech. 36 (1) (2012) 3–4, https://doi.org/10.1111/j.1747-1567.2011.00798.x.
[45] C. Nonis, C. Niezrecki, T.-Y. Yu, S. Ahmed, C.-F. Su, T. Schmidt, Structural health monitoring of bridges using digital image correlation, T. Kundu, ed., (2013), p. 869507. doi: 10.1117/12.2009647.
[46] P. Neri, A. Paoli, A.V. Razionale, C. Santus, Low-speed cameras system for 3D-DIC vibration measurements in the KHz range, Mech. Syst. Signal Process. 162 (2022) 108040, https://doi.org/10.1016/j.ymssp.2021.108040.
[47] D. Mastrodicasa, E. Di Lorenzo, S. Manzato, B. Peeters, P. Guillaume, 3D-DIC full field experimental modal analysis of a demo airplane by using low-speed cameras and a reconstruction approach, Mech. Syst. Signal Process. 227 (2025) 112387, https://doi.org/10.1016/j.ymssp.2025.112387.
[48] Y. Kato, S. Watahiki, M. Otaka, Full-field measurements of high-frequency micro-vibration under operational conditions using sub-nyquist-rate 3D-DIC and compressed sensing with order analysis, Mech. Syst. Signal Process. 224 (2025) 112179, https://doi.org/10.1016/j.ymssp.2024.112179.
[49] D. Botto, S. Occhipinti, C.M. Firrone, P. Neri, High-frequency nonlinear vibration analysis through low-frequency stereo-camera systems, Mech. Syst. Signal Process. 223 (2025) 111821, https://doi.org/10.1016/j.ymssp.2024.111821.
[50] T.J. Beberniss, D.A. Ehrhardt, High-speed 3D digital image correlation vibration measurement: recent advancements and noted limitations, Mech. Syst. Signal Pr. 86 (2017) 35–48.
[51] R.B. Berke, C.M. Sebastian, R. Chona, E.A. Patterson, J. Lambros, High temperature vibratory response of Hastelloy-X: stereo-DIC measurements and image decomposition analysis, Exp. Mech. 56 (2) (2016) 231–243, https://doi.org/10.1007/s11340-015-0092-3.
[52] P.L. Reu, D.P. Rohe, L.D. Jacobs, Comparison of DIC and LDV for practical vibration and modal, Mech. Syst. Signal Pr. 86 (2017) 2–16.
[53] R. Del Sal, L. Dal Bo, E. Turco, A. Fusiello, A. Zanarini, R. Rinaldo, P. Gardonio, Structural vibration measurement with multiple synchronous cameras, Mech. Syst. Signal Process. 157 (2021) 107742, https://doi.org/10.1016/j.ymssp.2021.107742.
[54] R. Hartley, A. Zisserman, Multiple view geometry in computer vision, Cambridge University Press, 2017.
[55] P.F. Sturm, S.J. Maybank, On plane-based camera calibration: a general algorithm, singularities, applications, Proceedings. 1999 IEEE Computer Society Conference on Computer Vision and Pattern Recognition (Cat. No PR00149), (1999), pp. 432–437. doi: 10.1109/CVPR.1999.786974.
[56] Z. Zhang, A flexible new technique for camera calibration, IEEE Trans. Pattern Anal. Mach. Intell. 22 (11) (2000) 1330–1334, https://doi.org/10.1109/34.888718.
[57] H.W. Kuhn, The hungarian method for the assignment problem, Naval Res. Logist. Quart. 2 (1–2) (1955) 83–97.
[58] L. Yu, B. Pan, Single-camera high-speed stereo-digital image correlation for full-field vibration measurement, Mech. Syst. Signal Pr. 94 (2017) 374–383.
[59] J. Javh, J. Slavič, M. Boltežar, Measuring full-field displacement spectral components using photographs taken with a DSLR camera via an analogue fourier integral, Mech. Syst. Signal Process. 100 (2018) 17–27, https://doi.org/10.1016/j.ymssp.2017.07.024.
[60] B. Pan, L. Yu, Q. Zhang, Review of single-camera stereo-digital image correlation techniques for full-field 3D shape and deformation measurement, Sci. China Technol. Sci. 61 (1) (2018) 2–20, https://doi.org/10.1007/s11431-017-9090-x.
[61] S. Barone, P. Neri, A. Paoli, A.V. Razionale, Low-frame-rate single camera system for 3D full-field high-frequency measurements, Mech. Syst. Signal Pr. 123 (2019) 143–152.
[62] D. Gorjup, J. Slavič, A. Babnik, M. Boltežar, Still-camera multiview spectral optical flow imaging for 3D operating-deflection-shape identification, Mech. Syst. Signal Process. 152 (2021) 107456, https://doi.org/10.1016/j.ymssp.2020.107456.
[63] F. Renaud, S. Lo Feudo, J.-L. Dion, A. Goeller, 3D vibrations reconstruction with only one camera, Mech. Syst. Signal Process. 162 (2022) 108032, https://doi.org/10.1016/j.ymssp.2021.108032.
[64] Y. Wang, W. Hu, J. Teng, Y. Xia, Full-field displacement measurement of long-span bridges using one camera and robust self-adaptive complex pyramid, Mech. Syst. Signal Process. 215 (2024) 111451, https://doi.org/10.1016/j.ymssp.2024.111451.
[65] Z. Su, L. Wang, J. Zheng, J. Zhang, Multi-view camera motion compensation in bridge displacement measurement with panoramic camera, Mech. Syst. Signal Process. 231 (2025) 112717, https://doi.org/10.1016/j.ymssp.2025.112717.
[66] W. Zhu, Z. Cui, L. Chen, Z. Zhou, X. Chu, S. Zhu, Robust monocular vision-based monitoring system for multi-target displacement measurement of bridges under complex backgrounds, Mech. Syst. Signal Process. 225 (2025) 112242, https://doi.org/10.1016/j.ymssp.2024.112242.
[67] D. Gorjup, J. Slavic, M. Boltezar, Frequency domain triangulation for full-field 3D-deflection-shape identification, Mech. Syst. Signal Pr. 133 (106287) (2019) 143–152.
[68] P. Gardonio, M.J. Brennan, Mobility and impedance methods in structural dynamics, in: F. Fahy, J. Walker (Eds.), Advanced Applications in Acoustics, Noise and Vibration, CRC Press, London, 2004.
[69] F. Moreno-Noguer, V. Lepetit, P. Fua, Accurate non-iterative O(n) solution to the PnP problem, in: 2007 IEEE 11th International Conference on Computer Vision, IEEE, 2007, pp. 1–8, https://doi.org/10.1109/ICCV.2007.4409116.
[70] S. Marburg, B. Nolte, (Eds.), Computational Acoustics of noise propagation in fluids - finite and boundary element methods, Springer Berlin Heidelberg, Berlin, Heidelberg, (2008). doi: 10.1007/978-3-540-77448-8.
[71] B. Lucas, T, Kanade, An iterative image registration technique with an application to stereo vision (IJCAI), (1981).
[72] V.C. Henríquez, P.M. Juhl, OpenBEM-an open source boundary element method software in acoustics, Internoise 2010, Sociedade Portuguesa de Acustica (SPA), Lisbon, (2010).
[73] S. Marburg, Discretization requirements: how many elements per wavelength are necessary?, Computational acoustics of noise propagation in fluids - finite and boundary element methods, Springer Berlin Heidelberg, Berlin, Heidelberg, pp. 309–332. doi: 10.1007/978-3-540-77448-8_12.
[74] S. Marburg, six boundary elements per wavelength: is that enough? J. Comput Acoust. 10 (01) (2002) 25–51, https://doi.org/10.1142/S0218396X02001401.
[75] P. Gardonio, E. Turco, Tuning of vibration absorbers and helmholtz resonators based on modal density/overlap parameters of distributed mechanical and acoustic systems, J. Sound Vib. 451 (2019) 32–70, https://doi.org/10.1016/j.jsv.2019.03.015.
[76] A. Peshave, F. Pierron, P. Lava, D. Moens, D. Vandepitte, Practical uncertainty quantification guidelines for DIC-based numerical model validation, Exp. Tech. 49 (3) (2025) 437–457, https://doi.org/10.1007/s40799-024-00758-1.
[77] J. Javh, J. Slavič, M. Boltežar, The subpixel resolution of optical-flow-based modal analysis, Mech. Syst. Signal Process. 88 (2017) 89–99, https://doi.org/10.1016/j.ymssp.2016.11.009.
[78] D. Gorjup, J. Slavič, M. Boltežar, Frequency domain triangulation for full-field 3D operating-deflection-shape identification, Mech. Syst. Signal Process. 133 (2019) 106287, https://doi.org/10.1016/j.ymssp.2019.106287.
[79] P.L. Reu, A study of the influence of calibration uncertainty on the global uncertainty for digital image correlation using a Monte Carlo approach, Exp. Mech. 53 (9) (2013) 1661–1680, https://doi.org/10.1007/s11340-013-9746-1.